An integrated technique for rapid gas permeability measurement of tight rock media

3   Tao Zhang[1], Qinhong Hu[1,2]*, Behzad Ghanbarian[32], Derek Elsworth[43], Zhiming Lu[54]

4   [1] Department of Earth and Environment Sciences, University of Texas at Arlington,
5   Arlington, TX 76019, United States

6   [2]National Key Laboratory of Deep Oil and Gas, China University of Petroleum (East
7   China), Qingdao 266580, P.R. China

8   [32] Porous Media Research Lab, Department of Geology, Kansas State University, Manhattan,
9   KS 66506, United States

10   [3-4] Department of Energy and Mineral Engineering, G3 Centre and Energy Institute, The
11   Pennsylvania State University, University Park, PA 16802, United States

12   [54] The Earth and Environmental Sciences Division, Los Alamos National Laboratory, Los
13   Alamos, NM 87544, United States

18   *Prepared for*

19   *Hydrology and Earth System Sciences*

20   ~~December~~ August 2~~6~~0, ~~2022~~2023

23   * Corresponding author: ~~max~~hu~~q~~inhong@u~~pc~~ta.edu.cn

Abstract: Nano-darcy level permeability measurements of porous media, such as nano-porous mudrocks, ~~are frequently conducted with gas invasion methods into granular-sized samples with short diffusion lengths and thereby reduced experimental duration~~are only practically feasible with gas invasion methods into granular-sized samples with short diffusion lengths and thereby reduced experimental duration; however, these methods lack rigorous solutions and standardized experimental procedures. For the first time, we resolve this by providing an integrated technique (termed as gas permeability technique) with coupled theoretical development, experimental procedures, and data interpretation workflow. Three exact mathematical solutions for transient and slightly compressible spherical flow, along with their asymptotic solutions, are developed for early- and late-time responses. Critically, one late-time solution is for an ultra-small gas-invadable volume, important for a wide range of practical usages. Developed as applicable to different sample characteristics (permeability, porosity, and mass) in relation to the storage capacity of experimental systems, these three solutions are evaluated from essential considerations of error difference between exact and approximate solutions, optimal experimental conditions, and experimental demonstration of mudrocks~~stone~~ and molecular-sieve samples. Moreover, a practical workflow of solution selection and data reduction to determine permeability

is presented by considering samples with different permeability and porosity under various granular sizes. Overall, this work establishes a rigorous, theory-based, rapid, and versatile gas permeability measurement technique for tight media at sub-nano darcy levels.

Keywords: permeability; granular samples; pulse-decay; mathematical solutions; experimental methods.

Highlights:

- An integrated (both theory and experiments) gas permeability technique (GPT) is presented.

- Exact and approximate solutions for three cases are developed with error discussion.

- Conditions of each mathematical solution are highlighted for critical parameters.

- Essential experimental methodologies and data processing procedures are provided and evaluated.

1. Introduction

Shales, crystalline, and salt rocks with low permeabilities (e.g., $<10^{-17}$ m^2 or 10 micro-darcies μD) are critical components to numerous subsurface studies. Notable examples are the remediation of contaminated sites(Neuzil, 1986; Yang et al., 2015), long-term performance of high-level nuclear waste repositories (Kim et al., 2011; Neuzil, 2013), enhanced geothermal systems (Huenges, 2016; Zhang et al., 2021), efficient development of unconventional oil and gas resources (Hu et al., 2015; Javadpour, 2009), long-term sealing for carbon utilization and storage (Fakher et al., 2020; Khosrokhavar, 2016), and high-volume and effective gas (hydrogen) storage (Liu et al., 2015; Tarkowski, 2019). For fractured rocks, the accurate characterization of rock matrix and its permeability is also critical for evaluating the effectiveness of low-permeability media, particularly when transport is dominated by slow processes like diffusion (Ghanbarian et al., 2016; Hu et al., 2012).

Standard permeability test procedures in both steady-state and pulse-decay methods use consolidated cm-sized core-plug samplescore-plug samples (e.g., 2.54 cm in diameter), which may contain fractures and show dual- or triple-porosity characteristics (Abdassah and Ershaghi, 1986; Bibby, 1981). The overall permeability may therefore be controlled by a few bedding-oriented or cross-cutting fractures, even if experiments are conducted at reservoir

79   pressures (Bock et al., 2010; Gensterblum et al., 2015; Gutierrez et al., 2000;

80   Luffel et al., 1993). Fractures might be naturally- or artificially-induced (e.g.,

81   created during sample processing), which makes a comparison of permeability

82   results among different samples difficult (Bock et al., 2010; Gensterblum et

83   al., 2015; Gutierrez et al., 2000; Luffel et al., 1993). Hence, methods for

84   measuring the matrix (non-fractured) permeability in tight media, with a

85   practical necessity of using granular samples, have attracted much attention to

86   eliminate the ~~confounding~~sides effect of fractures (Civan et al., 2013;

87   Egermann et al., 2005; Heller et al., 2014; Wu et al., 2020; Zhang et al., 2020).

88   A GRI (Gas Research Institute) method was developed by Luffel et al. (1993)

89   and followed by Guidry et al. (1996) to measure the matrix permeability of

90   crushed mudrocks (Guidry et al., 1996; Luffel et al., 1993). Such a method

91   makes permeability measurement feasible in tight and ultra-tight rocks (with

92   permeability $< 10^{-20}$ m^2 or 10 nano-dcarcies, nD), particularly when

93   permeability is close to the detection limit of the pulse-decay approach on core

94   plugs at ~10 nD (e.g., using commercial instrument of PoroPDP-200 of

95   CoreLab). In the GRI method, helium may be used as the testing fluid to

96   determine permeability on crushed samples at different sample sizes (e.g.,

97   within the 10-60 mesh range, which is from 0.67 mm to 2.03 mm). The limited

98   mesh size of 20-35 (500-841 μm in diameter) was recommended in earlier

works, which has led to the colloquial names of "the GRI method/size" in the literature (Cui et al., 2009; Kim et al., 2015; Peng and Loucks, 2016; Profice et al., 2012). However, Luffel et al. (Guidry et al., 1996; Luffel et al., 1993) did not document the processing methodologies needed to derive the permeability from experimental data from such a GRI method. That is, there are neither standard experimental procedures for interpreting gas pulse-decay data in crushed rock samples nor detailed mathematical solutions available for data processing in the literature (Kim et al., 2015; Peng and Loucks, 2016; Profice et al., 2012). In this work, we achieve to: (1) develop mathematical solutions to interpret gas pulse-decay data in crushed rock samples without published algorithm available as this method shares different constitutive phenomena to the traditional pulse-decay method for core plug samples in Cartesian coordinates; and (2) present associated experimental methodology to measure permeability, reliably and reproducibly, in tight and ultra-tight granular media.

~~The rest of this article is organized as follows.~~ We first derive the constitutive equations for gas transport in granular (unconsolidated or crushed rock) samples. Specifically, we develop three mathematical solutions which cover different experimental situations and sample properties. As each solution shows its own pros and cons, we then in detail present the error

119   analyses for the derived exact and approximate solutions and discuss their

120   applicable requirements and parameter recommendation for practical usages.

121   This work aims to fill the knowledge gap of the granular rock (matrix)

122   permeability measurement and follow-on literature by establishing an

123   integrated methodology for reproducible measurements of nD-level

124   permeability in tight rock for emerging energy and resources subsurface

125   studies.

126   **2. Mathematical solutions for gas permeability of granular samples**

127   For a compressible fluid under unsteady-state conditions, flow in a porous

128   medium can be expressed by the mass conservation equation:

129
$$\frac{\partial p}{\partial t} + \nabla \cdot (\rho \overline{v}) = 0 \qquad (1A)$$

130   where p is the pressure, t is the time, ρ is the fluid density, and $\overline{v}$ is the

131   Darcy velocity. In continuity equations derived for gas flow in porous media,

132   permeability can be treated as a function of pressure through the ideal gas law.

133   Constitutive equations are commonly established for a small pressure

134   variation to avoid the non-linearity of gas (the liquid density to be a constant)

135   and to ensure that pressure would be the only unknown parameter (Haskett et

136   al., 1988). For spherical coordinates of fluid flow in porous media, assuming

137   flow along the radial direction of each spherical solid grain, Eq. (1A) becomes

138
$$\frac{\partial p}{\partial t} \phi = \frac{1}{c_t} \frac{k}{\mu r^2} \frac{\partial}{\partial r} \left(r^2 \frac{\partial p}{\partial r} \right) \qquad (1B)$$

139   The gas compressibility c_t is given by

140
$$c_t = \frac{1}{\rho} \frac{d\rho}{dp} = \frac{1}{p} - \frac{1}{z} \frac{dz}{dp} \qquad (1C)$$

141   In Eqs. (1B) and (1C), ϕ and k are sample porosity and permeability, r

142   is the migration distance of fluid, μ is the fluid viscosity, and z is the gas

143   deviation (compressibility) factor and is constant.

144   To correct for the non-ideality of the probing gas, we treat gas density as a

145   function of pressure and establish a relationship between the density and the

146   permeability through a pseudo-pressure variable (given in the 1st part of

147   Supplemental Information SI1). Detailed steps for deriving mathematical

148   solutions for the GPT can be found in SI2, based on heat transfer studies

149   (Carslaw and Jaeger, 1959). The Laplace transform , in combination with the

150   Bessel equation, is an efficient tool for solving gas transport in granular

151   samples with low permeabilities, as applied in this study. Alternatively, other

152   approaches, such as the Fourier analysis, Sturm-Liouville method, or Volterra

153   integral equation of the second form may be used (Carslaw and Jaeger, 1959;

154   Haggerty and Gorelick, 1995; Ruthven, 1984).

155   We applied dimensional variables to derive the constitutive equation given

156   in Eq. (S10) for which the initial and boundary conditions are

157
$$\frac{\partial^2 U_s}{\partial \xi^2} + s^2 U_s = 0 \Big|_{U_s=0, \xi=0} \qquad \text{(1D)(2A)}$$

158
$$\alpha^2 (U_s - 1) = \frac{3}{K_c}\left(\frac{\partial U_s}{\partial \xi} - \frac{U_s}{\xi}\right)\Big|_{\xi=1} \qquad \text{(1E)(2B)}$$

159 where U_s and ξ represent the dimensionless values of gas density and

160 sample scale, and s is the transformed Heaviside operator. α in Eq. (2B) is

161 determined by solving Eq. (S30) for its root. K_c in Eq. (2B)(1E) is a critical

162 parameter that represents the volumetric ratio of the total void volume of the

163 sample cell to the pore volume of the porous samples. It is similar to the

164 storage capacity, controlling the acceptable measurement range of

165 permeability and decay time, in the pulse-decay method proposed by Brace et

166 al. in (1986 8) (Brace et al., 1968).

167   The fractional gas transfer for the internal (limited K_c value) and external

168 (infinite K_c value) gas transfer of sample is given by

169
$$F_f = 1 - 6\sum_{n=1}^{\infty} \frac{K_c(1+K_c)e^{-\alpha_n^2 \tau}}{9(K_c+1) + \alpha_n^2 K_c^2} \qquad \text{(2C)}$$

170
$$F_s = 1 - \frac{6}{\pi^2}\sum_{n=1}^{\infty} \frac{e^{-(n\pi)^2 \tau}}{n^2} \qquad \text{(2D)}$$

171 where F_f and F_s represent the uptake rate of gas outside and inside the

172 sample separately as a dimensionless parameter, and τ is the Fourier number

173 of dimensionless time. Three approximate solutions of the transport

174   coefficient based on Eqs. (2C) and (2D) for various conditions are presented

175   below.

176   The late-time solution to Eq. (2C) for a limited K_c value (called LLT

177   hereafter) is

178
$$k = \frac{R_a{}^2 \mu c_t \phi_f s_1}{\alpha_1{}^2} \qquad (3A)$$

179   The late-time solution to Eq. (2D) when K_c tends to infinity (ILT hereafter)
180   is

181
$$k = \frac{R_a{}^2 \mu c_t \phi_f s_2}{\pi^2} \qquad (3B)$$

182   The early-time solution to Eq. (2D) when K_c approaches infinity (IET
183   hereafter) is

184
$$k = \frac{\pi R_a{}^2 \mu c_t \phi_f s_3}{36} \qquad (3C)$$

185   In Eq. (3), R_a is the particle diameter of a sample, and s_1, s_2, and s_3 are

186   the three exponents that may be determined from the slopes of data on double

187   logarithmic plots. Table 1 summarizes Eqs. (3A) to (3C) and conditions under

188   which such approximate solutions would be valid.

189   Table 1. Solutions schematic with difference K_c and τ values

Parameter	Symbol	Remarks		
Volume fraction§	K_c	Limited value for $K_c < 10$	Infinity value for $K_c > 10$	
Exact. Density fraction£	F	F_f	F_s	
Approx. Solution of Density fraction*	Eqs. (3A-3B)	Eq. (3A) (LLT)	Eq. (3C) (IET)	Eq. (3B)) (ILT)
Available Dimensionless time for Approx. solution	τ	Late-time solution $\tau > 0.024$	Early-time solution $\tau < 0.024$	Late-time solution $\tau > 0.024$

§ It defines as the volumetric ratio of the total void volume of the sample cell to the pore volume of the porous samples, the classification between the limited and infinity value is proposed as 50 with the following analyses.

£ The original constitutive equation for different K_c value.

* Eqs. (3A-3C) are three approximate solutions of density faction function F.

190   Based on diffusion phenomenology, Cui et al. (2009) presented two

191   mathematical solutions similar to our Eqs. (3A) and (3C). In the work of Cui

192   et al. (2009), however, one of late-time solution is missing, and error analyses

193   are not provided. Besides, the lack of detailed analyses of τ and K_c in the

194   constitutive equations will likely deter the practical application of Eq. (3B),

195   which is able to cover an experimental condition of small sample mass with a

196   greater τ (further analyzed in Section 3). Furthermore, the early-time and

197   late-time solution criteria are not analyzed, and the pioneering work of Cui et

198   al. (2009) does not comprehensively assess practical applications of their two

199   solutions in real cases, which is addressed in this study~~Based on diffusion~~

200   ~~phenomenology, Cui et al. (2009) presented two mathematical solutions~~

201   ~~similar to our Eqs. (3A) and (3C). In the work of Cui et al. (2009), however,~~

202   ~~the lack of detailed analyses of τ and K_c in the constitutive equations may~~

203   ~~deter the practical application of Eq. (3B), which is unable to cover an~~

204   ~~experimental condition of small sample mass with a greater τ (further~~

205   ~~analyzed in section 3). In addition to that, Cui et al. (2009) did not~~

206   ~~comprehensively assess practical applications of their two solutions, which is~~

207   ~~addressed in this study~~. Hereafter, we refer to the developed mathematical and

208   experimental, gas-permeability-measurement approach holistically as gas

209   permeability technique (GPT).

3. Practical usages of algorithms for the GPT

211   As aforementioned, mathematical solutions given in Eqs. (3A) and (3B)

212   were deduced based on different values of K_c and τ as shown in the SI2.

213   This means each solution holds only under specific experimental conditions,

214   which are mostly determined by the permeability, porosity, and mass of

215   samples, as well as gas pressure and void volume of the sample cell. In this

216   section, the influence of parameters K_c and τ on the solution of constitutive

217   equation is analyzed and a specific value of dimensionless time ($\tau = 0.024$) is

218   proposed as the criterion required to detect the early-time regime from the late-

219   time one for the first time in the literature. We also demonstrate that the early-

220   time solution of Eq. (3C), which has been less considered for practical

221   applications in previous studies, is also suitable and unique under common

222   situations. Besides, the error of the approximate solution compared to the

223   exact solution and their capabilities are discussed, as it helps to select an

224   appropriate mathematical solution at small τ values. Moreover, we showcase

225   the unique applicability and feasibility of the new solution of Eq. (3B).

3.1 Sensitivity analyses of the K_c value for data quality control

227   To apply the GPT method, appropriately selecting the parameter K_c in Eqs.

228   (3A)-(3C) is crucial, as it is a critical value for data quality control. Recall that

229 ~~K_c represents the volumetric ratio of the total void volume of the sample cell~~

230 ~~to the pore volume of the porous samples.~~ The dimensionless density outside

231 the sample, U_f, is related to K_c via Eq. (S33) in the SI2. One may simplify

232 Eq. (S33) by replacing the series term with some finite positive value and set

233
$$U_f - \frac{K_c}{1+K_c} > 0 \qquad\qquad (1G)$$

234 We define $K_f = K_c/(1 + K_c)$ to interpret the density variance of the system

235 as K_f is closely related to the dimensionless density outside the sample, U_f.

236 Eq. (1G) shows the relationship between the U_f and K_c (~~plotted in~~ Fig.

237 1). For $K_c > 0$, K_f falls between 0 and 1. The greater the K_f value is, the

238 insensitive to density changes the system would be. For K_c equal to 50 ~~(not~~

239 ~~shown in Fig. 1)~~, K_f would no longer be sensitive to K_c variations as it has

240 already approached 98% of the dimensionless density. This means that the U_f

241 value needs to be greater than 0.98, and this leaves only 2% of the fractional

242 value of U_f available for capturing gas density change. When K_c is 100, the

243 left fractional value of U_f would be 1%. This would limit the amount of data

244 available (the linear range in Fig. S1) for the permeability calculation, which

245 would complicate the data processing. Thus, for the GPT experiments, a small

246 value of K_c (less than 10) is recommended, as K_f nearly reaches its plateau

247 beyond $K_c = 10$ (Fig. 1). When K_c is 10, the left fractional value of U_f is

248   only as low as 9%.
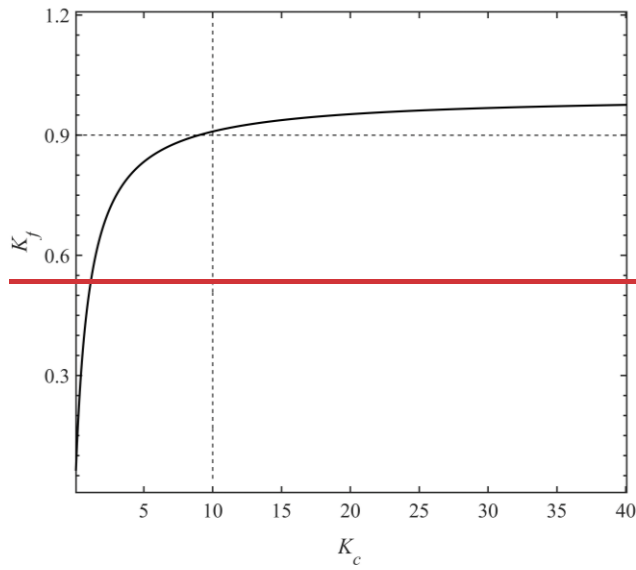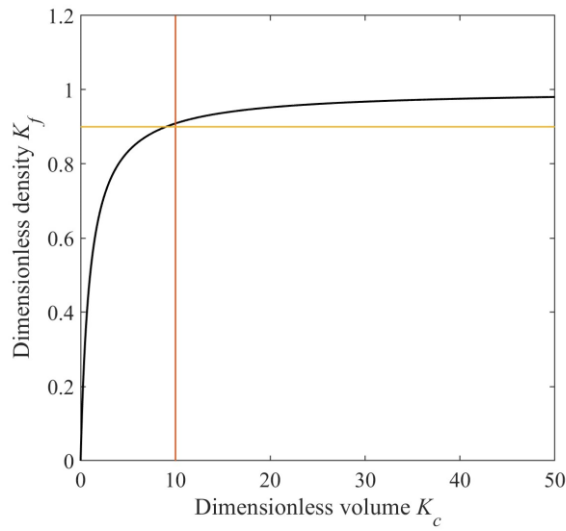
Fig. 1. Dimensionless density, K_f, as a function of dimensionless volume K_c.

~~Recall that $K_f = K_c/(1 + K_c)$.~~ Major variations in K_f occur for $K_c < 10$ indicating

longer gas transmission duration with more pressure-decay data available for

254   permeability derivation.

255

3.2 Recommendation for solution selection

257   The following three aspects need to be considered before selecting the
258   appropriate solution for permeability calculation: 1) ~~selecting~~ early- or late-
259   time solutions; 2) error between the approximate and exact solutions; and 3)
260   the convenience and applicability of solutions suitable for different
261   experiments. We will first discuss the selection criteria for early- or late-time
262   solutions.

263   Fig. 2(a) shows the exact solution of F_s with their two approximate early-
264   and late-time solution (Table 1). Two exact solutions of F_f ~~for~~ where K_c
265   equals to 10~~,~~ or 50 are also demonstrated in Fig. 2(a). Fig. 2(b) depicts the
266   exact solution from F_f for different K_c values from 1 to 100 and their
267   corresponding approximate solution for Eq. (3A). The intersection point of the
268   solution Eq. (3B) and Eq. (3C), namely $\tau = 0.024$ in Fig. 2(a), is used for
269   distinguishing early- and late-time solutions.

270   Two notable observations can be drawn from Fig. 2(b). Firstly, the
271   approximate solution Eq. (3A) would only be applicable at late times when
272   τ is longer than 0.024. For $\tau < 0.024$, regardless of the K_c value, Eq. (3C)
273   would be more precise than Eqs. (3A) and (3B) and return results close to the

exact solution for both F_f and F_s. Secondly, results of Eqs. (3A) and (3B)

presented in Fig. 2(a) are similar; ~~there is only a minor difference but become~~

~~very close at greater K_c values~~there difference is very small especially

for $K_c > 10$. Due to the fact that core samples from deep wells are relatively

short in length and their void volume is small (ultra-low porosity and

permeability such as in mudrocks~~stones~~ with $k \le 0.1$ nD), in practice, a

solution for $10 < K_c < 100$ is the most common outcome, even if the sample

cell is loaded as full as possible. Under such circumstances, the newly derived

solution, Eq. (3B), becomes practical and convenient: 1) if the K_c and

dimensionless time τ have not been evaluated precisely before the GPT

experiment, this solution may fit most experimental situations; 2) this solution

is suitable for calculation as it does not need the solution from the

transcendental equation of Eq. (S30) because the denominator of α has been

replaced by π. The data quality control is discussed in Section 4.1.
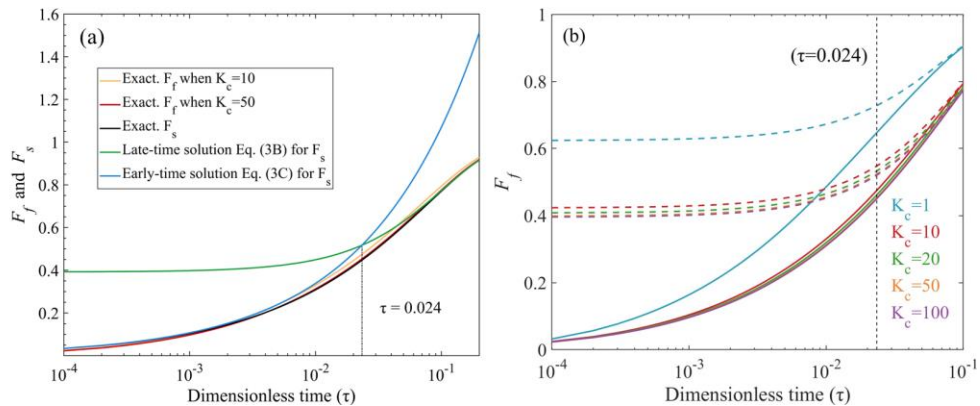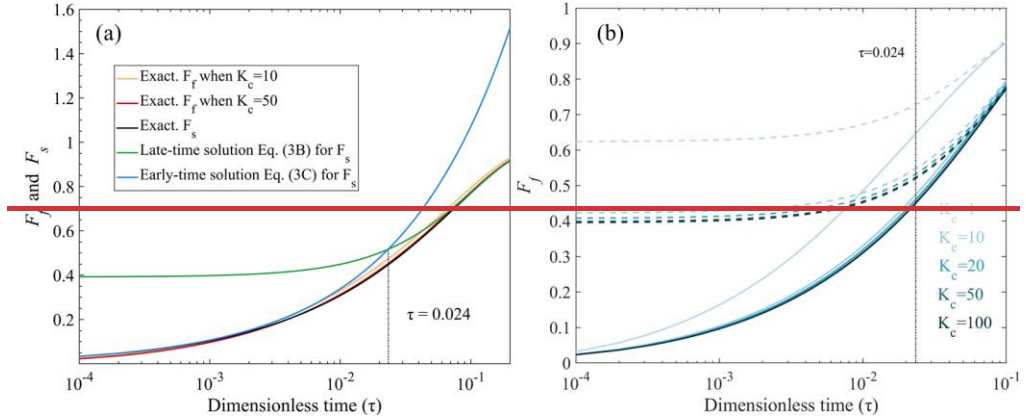
Fig. 2. Three GPT solutions with different values of τ, K_c; the dashed lines are approximate solutions without a series expansion in Fig. (2b) for F_f. Figure modified from Cui et al. (2009).

3.3 Applicability of the early-time solution

A small K_c value can guarantee a sufficient time for gas transfer in samples and provide enough linear data for fitting purposes. We note that the selection of the limited K_c solution of F_f, and the infinity K_c solution F_s is controlled by K_c. However, before the selection of K_c, the dimensionless time is the basic parameter to be estimated as a priori before the early- or late-time solutions are selected.

For pulse-decay methods, the early-time solution has the advantage of capturing the anisotropic information contained in reservoir rocks (Jia et al., 2019; Kamath, 1992). However, it suffers from the shortcoming of uncertainty

303 in data for initial several seconds, which as a result is not recommended for

304 data processing (Brace et al., 1968; Cui et al., 2009). This is due to: (1) the

305 Joule-Thompson effect, which causes a decrease in gas temperature from the

306 expansion; (2) kinetic energy loss during adiabatic expansion; and (3) collision

307 between molecules and the container wall. These uncertainties normally

308 ~~happen~~ occur in the first 10-30 sec, shown in our experiments as a fluctuating

309 period called "Early Stage".

310   However, the "Early Stage" present in pulse-decay experiments does not

311 mean that the early-time solution is not applicable. We demonstrate the

312 relationship between time and dimensionless time in Fig. 3 that a short

313 dimensionless time may correspond to a long testing period of hundred to

314 thousand seconds in experiments. This is particularly noticeable for the. ~~For~~

315 ~~example,~~ ultra-low permeability samples with $k \leq$ 0.1 nD and small

316 dimensionless times $\tau < 0.024$. This situation would only be applicable to

317 early-time solution, but with data available beyond the "Early Stage" and

318 provide available data in a long time (hundreds to thousands of seconds). For

319 example, the early-time solution would fit ultra-low permeability samples in

320 600s ~~around~~ for 0.1 nD, and at least 1000s for 0.01 nD shown in Fig. 3 in the

321 region below the dark line. Then, using Eq. (3C), the derived permeability

322 would be closer to its exact solution in the earlier testing time (but still after

323 the "Early Stage"). The mudrock samples that we tested, with results presented

324 in Section 5.3, exhibit low permeabilities, approximately on the order of 0.1

325 nD.For mudrock samples that we have tested (results presented in Section 5.3),

326 permeabilities are low and in the order of 0.1 nD.

327
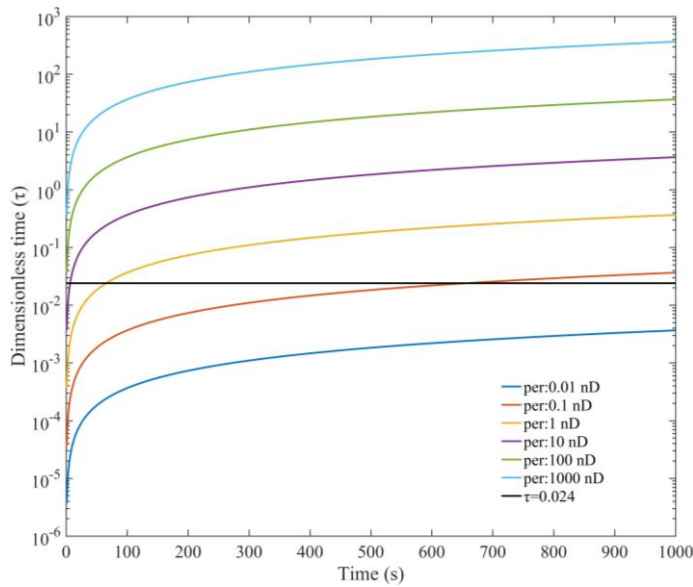
328 Fig. 3 Dimensionless time τ versus actual times for different permeability values

329 trough Eq. (S14) using He gas, sample porosity of 5%, and sample diameter of 2

330 mm.

3.4 Error analyses between exact and approximate solutions

332 It is unpractical to use the exact solutions with their series part to do the

333   permeability calculation; thus, only the approximate solutions are used and the

334   error difference between the exact and approximate solutions is discussed here.

335   The original mathematical solutions, Eqs. (S39) and (S49), are based on

336   series expansion. For dimensionless densities F_f and F_s in Eqs. (S39) and

337   (S49), their series expansion terms should converge. However, the rate of

338   convergence is closely related to the value of τ. For example, from Eq. (S30),

339   when $\tau \geq 1$, the exponent parts of U_s and U_f are at least $(2n + 1)\pi^2$.

340   Therefore, the entire series expansion term can be omitted without being

341   influenced by K_c. In practical applications, the solutions given in Eqs. (3A)-

342   (3C) are approximates without series expansion. In this study, we provide the

343   diagrams of change in errors with dimensionless time in the presence of

344   adsorption (Fig. 4).

345   For F_f, the error differences between the exact and approximate solutions

346   are 3.5% and 0.37% for $\tau = 0.05$ and 0.1 when $K_c = 10$, respectively. When

347    $\tau \leq 0.024$, the error would be greater than 14.7%. Fig. 2(b) shows that F_f

348   can be approximated as F_s when K_c is greater than 10; the error difference

349   between F_f and F_s is quite small at this K_c value (for $K_c = 10$, 6.6% is the

350   maximum error when $\tau = 0.01$; 4.4% when $\tau = 0.05$; and 2.9% when $\tau = 0.1$)

351   as shown in Fig. 4.

352 For F_s, the error difference is roughly the same as F_f and equal to 3.6%

353 for $\tau = 0.05$ and 0.38% for $\tau = 0.1$. This verifies that newly derived Eq. (3B)

354 is equivalent to Eq. (3A) when K_c is greater than 10. As for the evaluation

355 of Eq. (3C), the error difference with the exact solution will increase with

356 dimensionless time (5.1% for $\tau = 0.003$, 9.7% for $\tau = 0.01$, and 16% for $\tau =$

357 0.024).

358
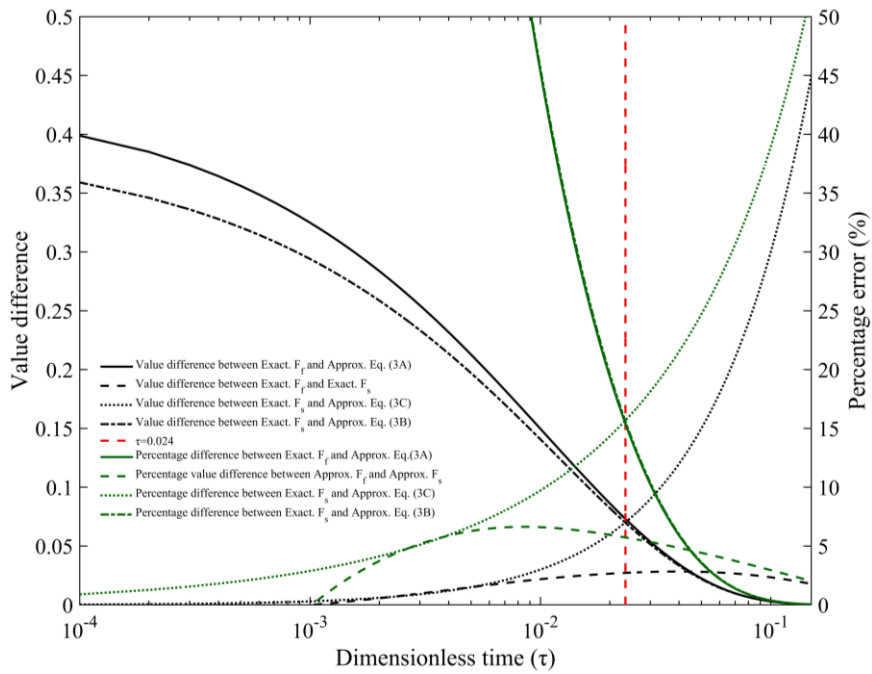
359 Fig. 4. Error analyses of F_f and F_s for their exact and approximate solutions

360 ~~In the following, we apply the approximate solutions, Eqs. (3A-3C), to~~

361 ~~some detailed experimental data and determine permeability in several shale~~

362 ~~samples practically compatible with sample size, gases, and molecular~~

363 ~~dynamics analyses.~~

4. Influence of kinetic energy on gas transport behavior

4.1 Flow state of gas in granular samples

In the following, we apply the approximate solutions, Eqs. (3A-3C), to some detailed experimental data and determine permeability in several ~~shale~~mudrock~~stone~~ samples practically compatible with sample size, gases, and molecular dynamics analyses.

During the GPT, with the boundary conditions described in SI2, the pressure variation is captured after gas starts to permeate into the sample from the edge, and the model does not take into account the gas transport between particles or into any micro-fractures, if available. Thus, the transport that conforms to the "unipore" model and occurs after the "Early Stage" (defined in Section 3.3) ~~and~~ or during the "Penetration Zone" (the area between the two vertical lines in Fig. 5), should be used to determine the slope. ~~See~~ Fig. S2 ~~in which it is shown~~shows how to obtain the permeability result using the applicable mathematical solutions (Eqs. 3A-C). Fig. 5 shows the pressure variance with time during the experiment using ~~different~~ sample size from 0.34 mm to 5.18 mm for sample X-1 and s~~. Similar pattern was observed for s~~ample X-2 ~~as well~~. From Fig. 5, the time needed to reach pressure equilibrium after the initial fluctuation stage is 20-100 sec, and the "Penetration Zone" decreases with decreasing grain size over this time period.

384
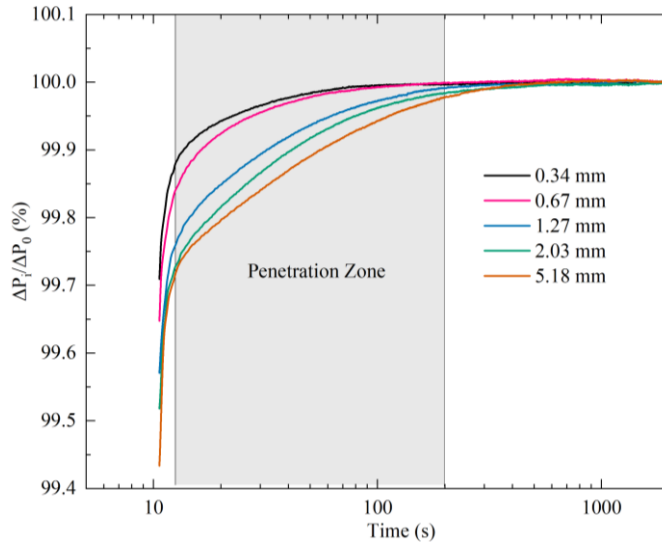
Fig. 5. Fitting region (the "Penetration Zone" in the shadowed area) for mudrock

sample X-1 with different granular sizes; the penetration zone illustrating the

pressure gradient mainly happens at 20 to 200 sec for this sample.

In fact, the "Penetration Zone", as an empirical period, is evaluated by the

pressure change over a unit of time before gas is completely transported into

the inner central part of the sample to reach the final pressure. Owing to the

sample size limitation, a decreasing pressure could cause multiple flow states

(based on the Knudsen number) to exist in the experiment. The pressure during

the GPT experiment varies between 50 and 200 psi (0.345 MPa to 1.38 MPa).

Fig. 6 shows the Knudsen number calculated from different pressure

conditions and pore diameters together with their potential flow state. Based

on Fig. 6, the flow state of gas in the GPT experiments is mainly dominated

398 by Fickian and transition diffusion. Essentially, the flow state change with

399 pressure should be strictly evaluated through the Knudsen number in Fig. 6 to

400 guarantee that the data in the "Penetration Zone" are always fitted with the

401 GPT's constitutive equation for laminar or diffusive states. This helps obtain a

402 linear trend for $ln(1 - F_f)$ or $F_s{}^2$ versus time for low-permeability media.

403 Experimentally, data from 30 to several 100 seconds are recommended for

404 tight rocks like shales within the GPT methodology.

405
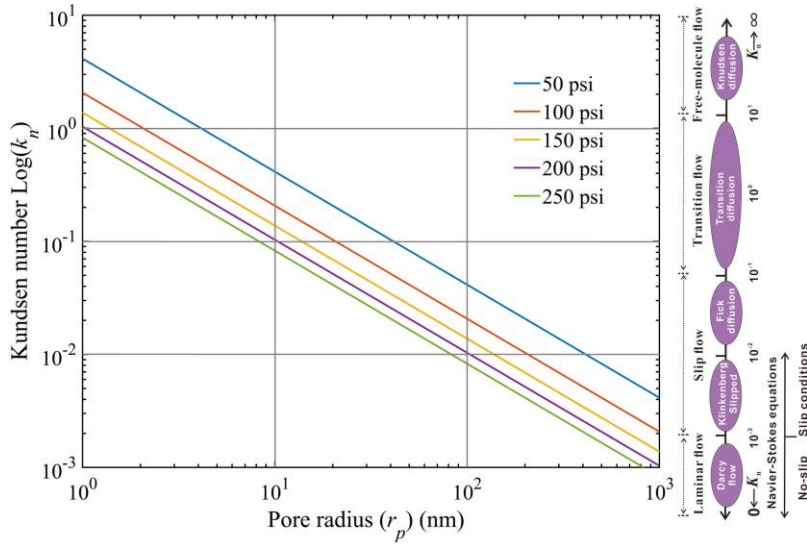
406 Fig. 6. Flow state of gas under diffferent testing pressures; modified from Chen &

407 Pfender (1983) and Roy et al. (2003) (Chen and Pfender, 1983; Roy et al., 2003).

408

409 In the GPT approach, as mentioned earlier, Eq. (S33) holds for small K_c

410 values (e.g., < 10) so that the approximately equivalent void volume in the

411   sample cell and sample pore volume would allow for sufficient pressure drop.

412   It also gives time and allows the probing gas to expand into the matrix pores

413   to have a valid "Penetration Zone" and to determine the permeability. Greater

414   values of K_c would prevent the gas flow from entering into a slippage state

415   as the pressure difference would increase with increasing K_c. However, large

416   pressure changes would result in a turbulent flow (Fig. 6), which would cause

417   the flow state of gas to be no longer valid for the constitutive equation of the

418   GPT. Overall, the GPT solutions would be applicable to the gas permeability

419   measurement, based on the diffusion-like process, from laminar flow to

420   Fickian diffusion, after the correction of the slippage effect. ~~Though the liquid~~

421   ~~permeability is not complicated by the gas slippage effect, the liquid test is~~

422   ~~difficult in achieving the flow state of Knudsen number greater than 10^{-3},~~

423   ~~which normally occurs in the ultra-low permeability media. Therefore, gases~~

424   ~~are chosen, and practically needed, as the testing fluid in this work.~~

425   **4.2 Pressure decay behavior of four different probing gases**

426   We used three inert gases, including He, N_2, and Ar, and one sorptive gas

427   i.e., CO_2 (Busch et al., 2008), to compare the pressure drop behavior for

428   sample size with an average granular diameter of 0.675 mm~~behavior for~~

429   ~~sample size of 0.675 mm (average granular diameter)~~. Results for the mudrock

430   sample X-2 are presented in Fig. 7. Among the three inert gases, helium and

431   argon required the shortest and longest time to reach pressure equilibrium (i.e.,

432   He<N_2<Ar). In terms of pressure drop, argon exhibited the most significant

433   decrease.~~For pressure range, argon had the greatest pressure drop.~~ In a

434   constant-temperature system, the speed (or rate) at which gas molecules move

435   is inversely proportional to the square root of their molar masses. Hence, it is

436   reasonable that helium (with the smallest kinetic diameter of 0.21 nm) has the

437   shortest equilibrium time. However, the pressure drop is more critical than the

438   time needed to reach equilibrium for the GPT, as the equilibrium time does not

439   differ much (basically within 10 seconds for a given sample weight, except for

440   the adsorptive CO_2). Argon may provide a wider range of valid Penetration

441   Zones in a short time scale for its longest decay time except for adsorbed gas

442   of CO_2; a choice of inert and economical gas is suggested for the GPT

443   experiments.

444
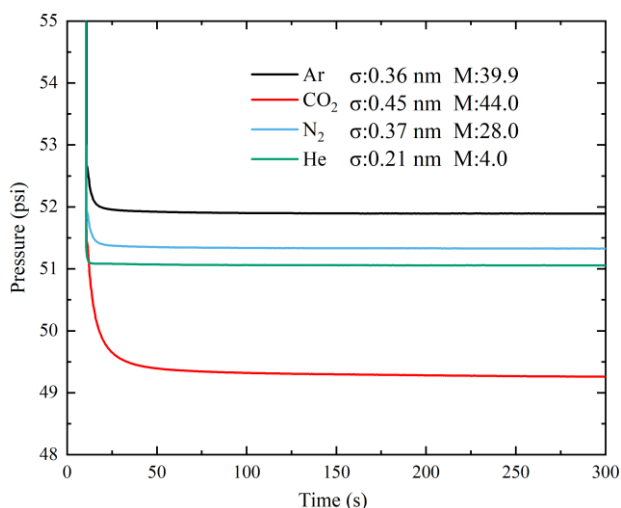
Fig. 7. Measured pressure decay curves from mudrock Sample X-2 for gases of different molecular diameters σ and molecular weights M (g/mol).

Fig. 7 shows that the pressure decay curve of the adsorptive gas CO_2 is different from those of the inert gases used in this study. CO_2 has a slow equilibrium ~~time~~ process due to its large molar mass, and the greatest pressure drop among the four gases due to its adsorption effect. This additional flux needs to be taken into account to obtain an accurate transport coefficient. ~~Adsorption of CO_2 is stronger than that of CH_4, especially in micropores in tight reservoirs (Busch et al., 2008).~~ Accordingly, multiple studies including laboratory experiments (Pini, 2014) and long-term field observations (Haszeldine et al., 2006; Lu et al., 2009) were carried out to assess the sealing efficiency of mudrocks~~rocks~~ for CO_2 storage. In fact, the GPT can supply a quick and effective way to identify the adsorption behavior of different mudrocks~~rocks~~ for both laminar-flow and diffusion states.

4.3 Pressure decay behavior for different granular sizes

We compared the pressure drop behavior of gas in the mudrock~~stone~~ Sample X-1 with different granular sizes (averaged from 0.34 mm to 5.18 mm) using the same sample weight and K_c. Results based on the experimental data shown in Fig. 8 indicate that a larger-sized sample would provide more data

465 to be analyzed for determining the permeability~~would provide more~~

466 ~~analyzable data to determine the permeability~~. This ~~because~~is because the

467 larger the granular size, and (1) the larger the pressure drop, (2) the longer the

468 decay time as Fig. 8 demonstrates. Th~~e~~is is consistent with the simulated

469 results reported by Profice et al. (2012) ~~(Profice et al., 2012)~~.

470
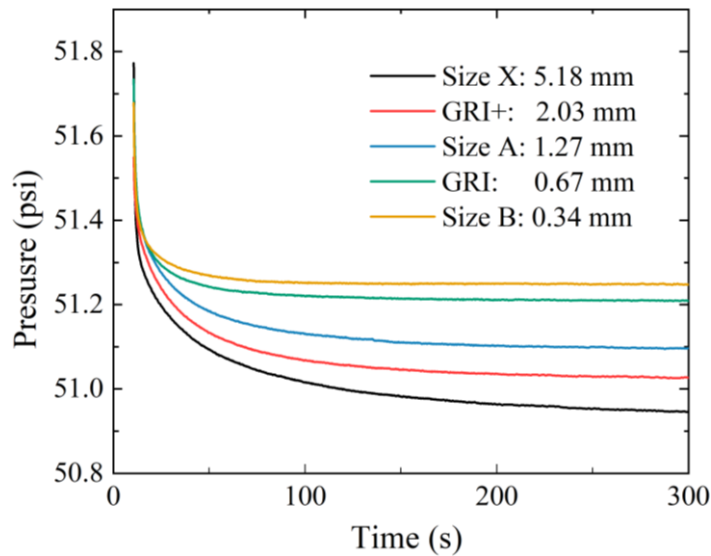
471 Fig. 8. Pressure decay curves measured by helium on sample X-1 with five different

472 granular sizes. The intra-granular porosity was 5.8% independently measured by

473 mercury intrusion porosimetry.

474

475 Table 2. Permeability results from the methods of GPT and SMP-200 for X-1.

Granular Size (mm)	SMP-200 (nD)[§]	GPT test 1 (nD)[£]	GPT test 2 (nD)[£]	Average value (nD)[£]	Fitting duration (s)	Unselected Solution (nD)*~~-type~~	Dimensionless time	Particle density (g/cm^{3})
5.18	-	1.17	1.17	1.17(ILT)	50-100	239(IET) 1.31(LLT)~~ILT~~	0.023-0.027	2.631
2.03	14.2	0.45	0.41	0.43(LLT)	50-100	11.1(IET) 0.36(ILT)~~LLT~~	0.026-0.028	2.626
1.27	-	0.10	0.10	0.10(ILT)	30-60	20.5(IET) 0.09(ILT)~~ILT~~	CR*	2.673

| 0.67 | 0.65 | 0.08 | 0.04 | 0.06(LLT) | 30-60 | 1570(IET) 0.03(ILT)~~LLT~~ | CR* | 2.658 |
| 0.34 | - | 0.02 | - | 0.02(IET) | 30-60 | 0.00076(LLT) 0.00068(BLT)~~IET~~ | CR* | 2.643 |

[§] The results are from the SMP-200 using the GRI default method.

[£] The results are from the GPT method we proposed.

[*] CR means the conflict results that the verified dimensionless time does not confirm the early- or late-time solutions using the solved permeability. For example, the verified dimensionless time would be > 0.024 using the early-time solution solved result and vice versa.

* represents the result which failed for the criteria of dimensionless time

476   As reported in Table 2, the permeability values measured by the GPT

477   method are one or two orders of magnitude greater than those measured by the

478   SMP-200 instrument. The built-in functions of SMP-200 can only be used for

479   two default granular sizes (500-841 μm for GRI and 1.70-2.38 mm for what

480   we call GRI+) to manually curve-fit the pressure decay data and determine the

481   permeability. The GRI method built in the SMP-200 only suggests the fitting

482   procedure for data processing without publicly available details of underlying

483   mathematics. The intra-granular permeabilities of mudrocks~~rock~~ sample X-1

484   vary from 0.02 to 1.17 nD for five different granular sizes using the GPT. With

485   the same pressure decay data selected from 30 to 200 sec, the permeability

486   results for GRI and GRI+ sample sizes from the SMP-200 fitting are 0.65 and

487   14.2 nD, as compared to 0.06 and 0.43 nD determined by the GPT using the

488   same mean granular size. Our results are consistent with those reported by

489   Peng & Loucks (2016) who found two to three orders of magnitude differences

490   between the GPT and SMP-200 methods (Peng and Loucks, 2016).

491   There exist several issues associated with granular samples with

492 diameters smaller than ~~Size A~~ (on average ~~diameter of~~ 1.27 mm~~)~~. First, the

493 testing duration is short, and second, there would not be sufficient pressure

494 variation analyzed in Fig. 8. Both may cause significant uncertainties in the

495 permeability calculation and, therefore, make samples with diameters smaller

496 than ~~Size A~~1.27 mm unfavorable for the GPT method, particularly extra-tight

497 (sub-nD levels) samples, as there is almost no laminar or diffusion flow state

498 to be captured. The greater pressure drop for larger-sized granular samples

499 would result in greater pressure variation and wider data region compared to

500 smaller granular sizes (see Figs. 6 and 9). Although samples of large granular

501 sizes   may   potentially   contain   micro-fractures,   which   complicate   the

502 determination of true matrix permeability (Heller et al., 2014), the versatile

503 GPT method can still provide size-dependent permeabilities for a wide range

504 of samples (e.g., from sub-mm to 10 cm diameter full-size cores) (Ghanbarian,

505 2022a, b). Besides, the surface roughness of large grains may also complicate

506 the determination of permeability, which need to pay attention to (Devegowda,

507 2015; Rasmuson, 1985; Ruthven and Loughlin, 1971). Overall, our results

508 demonstrated that sample diameters larger 2 mm are recommended for the

509 GPT to determine the nD permeability of tight mudrocks ~~or crystalline rocks~~,

510 while smaller sample sizes may produce uncertain results.

511 **4.4 Practical recommendations for the holistic GPT**

512   Here, we evaluate the potential approximate solution for tight rock

513   samples using frequently applied experimental settings by considering the

514   critical parameters, such as sample mass, porosity, and estimated permeability

515   (as compiled in Fig. 9 showing the dimensionless time versus porosity). Based

516   on the results presented in Figs. 3 and 6, only $t < 200s$ is dominant and critical

517   for the analyses of dimensionless time and penetration zone. Thus, we take

518   200s and use helium to calculate the dimensionless time. Another critical

519   parameter to assure enough decay data is the sample diameter greater than 2

520   mm. Thus, we only show the dimensionless time versus porosity for sample

521   diameter greater than the criteria of 2 mm.

522   Fig. 9 demonstrates that the sample permeability has dominant control on

523   the early- or late-solution selection, and we decipher a concise criterial for

524   three solutions selection. We classify the dimensionless time versus porosity

525   relationship into three cases. Firstly, among the curves shown in Fig. 9, only

526   that corresponding to $k = 0.1$ nD and sample diameter of 2 mm stays below

527   the dashed line representing $\tau = 0.024$. Therefore, the early time solution is

528   appropriate for tight samples with permeabilities less than 0.1 nD (as shown

529   in the analyses of Section 4.3, which also conforms to the situation of the

530   molecular sieve sample that we tested in SI3). Secondly, for permeabilities

531   greater than 10 nD (the curve is above the line of $\tau = 0.024$), the new derived

532   late-time solution, Eq. (3B), is recommended as it is more convenient for

533   mathematical calculation without the consideration of transcendental

534   functions. The reason is that the sample cell can be filled as much as possible

535   (~90% of the volume) with samples and solid objects. However, as the tight

536   rock hardly presents a large value of porosity, the small K_c value is difficult

537   to be achieved with an inconsequential influence between Eq. (3B) and Eq.

538   (3A). Lastly, in the case of permeability around 1 nD, the value of porosity

539   would be critical in the selection of the early- or late-time solutions, as shown

540   in Fig. 9.

541
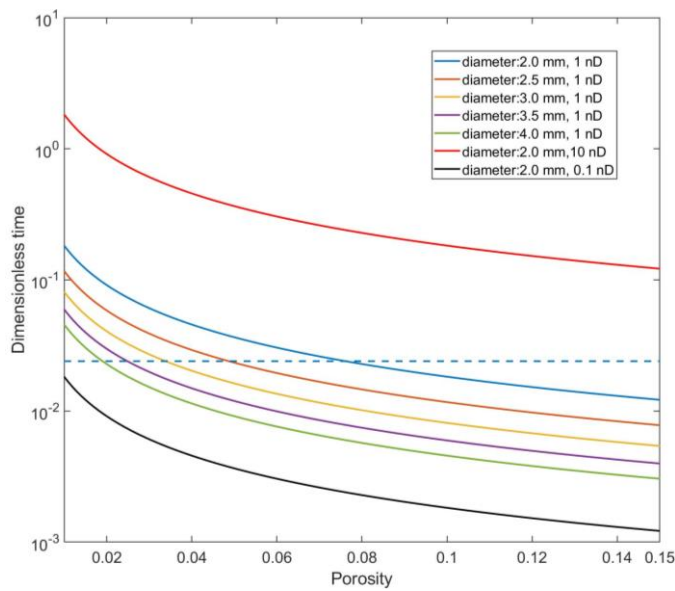
542   Fig. 9. Holistic GPT to explore the appropriate solution based on diameter,

543   permeability, and porosity of samples. The legend shows the diameter of granular

544   sample and permeability, along with a dashed line for dimensionless time of 0.024,

545   while regions above and below this value fit for the late- and early-time solutions,

546   respectively.

5. Conclusions

548   In the present work, we solved fluid flow state equation in granular porous

549   media and provided three exact mathematical solutions along with their

550   approximate ones for practical applications of low permeability measurements.

551   The mathematical solutions for the transport coefficient in the GPT were

552   derived for a spherical coordinate system, applicable from laminar flow to

553   ~~slippage correctedslippage~~-corrected Fickian diffusion. Of the three derived

554   solutions, one is valid during early times when the gas storage capacity K_c

555   approaches infinity, while the other two are late-time solutions to be valid

556   when K_c is either small or tends towards infinity. ~~Among the three~~

557   ~~derivations, one was early-time solution valid when gas storage capacity K_c~~

558   ~~approaches infinity and two were late-time solutions valid when either K_c is~~

559   ~~small or K_c tends to infinity.~~ We evaluated the derived solutions for a

560   systematic measurement of extra-low permeabilities in granular media and

561   crushed rocks using experimental methodologies with the data processing

562   procedures. We determined the error for each solution by comparing with the

563   exact solutions presented in the SI. The applicable conditions for such

564   solutions of the GPT were investigated, and we provided the selection

565   strategies for three approximate solutions based the range of sample

permeability. In addition, a detailed utilization of GTP was given to build up the confidence in the GPT method through the molecular sieve sample, as it enables a rapid permeability test for ultra-tight rock samples in just tens to hundreds of seconds, with good repeatability.

Data availability. This work did not use any data from previously published sources, and our experimental data & processing codes of MATLAB are available at https://doi.org/10.18738/T8/YZJS7Y, managed by Mavs Dataverse of the University of Texas at Arlington.

Supplement. An early-version preprint of this work appears as DOI: 10.1002/essoar.10506690.2 (Zhang et al., 2021).

Author contributions. TZ and QHH planned and designed the research, performed the analyses, and wrote the paper with contributions from all co-authors. BG, DK, and ZM participated in the research and edited the paper.

Competing interest. We declare that we do not have any commercial or associative interest that represents a conflict of interest in connection with the work submitted.

Acknowledgments. Financial assistance for this work was provided by the National Natural Science Foundation of China (41830431; 41821002), Shandong Provincial Major Type Grant for Research and Development from the Department of Science & Technology of Shandong Province (2020ZLYS08), Maverick Science Graduate Research Fellowship for 2022-2023, the AAPG and the West Texas Geological Foundation Adams Scholarships, and Kansas State University through faculty start-up funds to BG. We extend our deepest appreciation to handling editor Monica Riva for

590   her diligent assistance, and to the two anonymous referees for their insightful

591   comments on this paper.

592

Nomenclature

B_{ij} Correction parameter for viscosity, constant

c_t Fluid compressibility, Pa^{-1}

~~D Diffusion coefficient, m^2/s~~

F_f Uptake rate of gas outside the sample, dimensionless

F_s Uptake rate in the sample, dimensionless

f_1 Intercept of Eq. (S40), constant

~~J Physical flux, unit for certain physical phenomenon~~

K_a Apparent transport coefficient defined as Eq. (S9), m^2/s

K_c Ratio of gas storage capacity of the total void volume of the system to the pore (including adsorptive and non-adsorptive transport) volume of the sample, fraction

K_f Initial density state of the system, fraction

k Permeability, m^2

k_s Permeability defined as Eq. (S8), m^2/(pa·s)

L Coefficient, unit for certain physical transport phenomenon

M Molar mass, kg/kmol

M_m Molar mass of the mixed gas, kg/kmol

$M_{i,j}$ Molar mass for gas i or j, kg/kmol

M_s Total mass of sample, kg

N Particle number, constant

p Pressure, Pa

p_{cm} Virtual critical pressure of mixed gas, Pa

p_p Pseudo-pressure from Eq. (S1), Pa/s

R_a Particle diameter of sample, m

R Universal gas constant, 8.314 J/(mol·K)

619   r Diameter of sample, m

620   s_1 Slope of Eq. (S40), constant

621   s_2 Slope of function $Ln(1 - F_s)$, constant

622   s_3 Slope of function $F_s{}^2$, constant

623   T Temperature, K

624   T_{cm} Virtual critical temperature for mixed gas, K

625   t Time, s

626   U_f Dimensionless density of gas outside the sample, dimensionless

627   U_s Dimensionless density in grain, dimensionless

628   U_∞ Maximum density defined as Eq. (S37), dimensionless

629   V_1 Cell volume in upstream of pulse-decay method, m^3

630   V_2 Cell volume in downstream of pulse-decay method, m^3

631   V_b Bulk volume of sample, m^3

632   V_c Total system void volume except for sample bulk volume, m^3

633    $\overline{v}$ Dacian velocity in pore volume of porous media, m/s

634   X Pressure force, Pa

635    $y_{i,j}$ Molar fraction for gas i or j, fraction

636   z Gas deviation (compressibility) factor, constant

637   **Greek Letters:**

638   α_n The nth root of Eq. (S30), constant

639   μ Dynamic viscosity, pa·s or N·s/m^2

640    $\mu_{i,j}$ Dynamic viscosity for gas i or j, pa·s or N·s/m^2

641   μ_{mix} Dynamic viscosity of mixture gas, pa s or N s/m^2

642   μ_p Correction term for the viscosity with pressure, pa s or N s/m^2

643   ξ Dimensionless radius of sample, dimensionless

644   ρ Density of fluid, kg/m^3

645   ρ_0 Average gas density on the periphery of sample, kg/m^3

646   ρ_1 Gas density in reference cell, kg/m^3

647   ρ_2 Gas density in sample cell, kg/m^3

648   ρ_b Average bulk density for each particle, kg/m^3

649   ρ_f Density of gas changing with time outside sample, kg·m^{-3}·s^{-1}

650    $\rho_{f\infty}$ Maximum value of ρ_f defined as Eq. (S38), kg·m^{-3}·s^{-1}

651   ρ_p Pseudo-density from Eq. (S1), kg·m^{-3}·s^{-1}

652   ρ_s Density of gas changing with time in sample, kg·m^{-3}·s^{-1}

653   ρ_{ps} Pseudo-density of gas changing with time in sample, kg·m^{-3}·s^{-1}

654   ρ_{pf} Pseudo-density of gas changing with time outside sample, kg·m^{-3}·s^{-1}

655   ρ_{p2} Initial pseudo-density of gas in sample, kg·m^{-3}·s^{-1}

656   ρ_{p0} Average pseudo-density of gas on sample periphery, kg·m^{-3}·s^{-1}

657   ρ_{rm} Relative density to the mixed gas, kg·m^{-3}·s^{-1}

658   ρ_{sav} Average value of ρ_{sr} defined as Eq. (S47), kg·m^{-3}·s^{-1}

659   ρ_{sr} Average value of pseudo-density of sample changing with diameter,
660   kg·m^{-3}·s^{-1}

661    $\rho_{s\infty}$ Maximum value of ρ_{sr} defined as Eq. (S46), kg·m^{-3}·s^{-1}

662   τ Dimensionless time, dimensionless

663   ϕ Sample porosity, fraction

664   ϕ_f Total porosity ($\phi_f = \phi_a + \phi_b$) occupied by both free and adsorptive
665   fluids, fraction

Supporting Information (SI)

SI1. Consideration of Non-linearity of Gas and Solutions for a Mixed Gas State

For gas flow, we can use a pseudo-pressure variable to linearize Eq. (2A) as μ and c_t are functions of pressure. The pseudo-pressure p_p is defined as (Haskett et al., 1988)

$$p_p = 2 \int_{p_0}^{p} \frac{p}{\mu z} \, d p \qquad (S1)$$

By combining Eq. (S1) with the ideal gas law, the pseudo-density may be expressed as

$$\rho_p = \frac{pM}{RT} = \frac{p^2 M}{\mu z RT} \qquad (S2)$$

Because viscosity and compressibility do not change significantly (less than 0.7%) between 200 psi and atmospheric pressures, Eq. (S2) can be simplified to

$$\rho_p = \frac{p^2 M}{RT} \qquad (S3)$$

Thus, the density change is replaced by the pseudo-density for a precise calibration by using pressure squared.

During the GPT experiment, different gases in the reference and sample cells may complicate the hydrodynamic equilibrium of gas, and consequently the expression of transport phenomena, as the viscosity and gas compressibility are in a mixed state. Therefore, during the GPT experiment

685   when a different gas exists between the reference and sample cells a, a mixed

686   viscosity should be used after the gas in reference cell is released into the

687   sample cell. The viscosity of mixture μ_{mix} under pressure in Eqs. (3A)-(3C)

688   can be calculated from (Brokaw, 1968; Sutherland, 1895)

689
$$\mu_{mix} = \sum \frac{\mu_i}{1+\frac{1}{y_i}(\sum_{\substack{j=1 \\ j \neq i}}^{n} B_{ij}y_j)} + \mu_p \qquad (S4)$$

690   B_{ij} is a correction parameter independent of gas composition and can be

691   expressed as

692
$$B_{ij} = \frac{[1+(\frac{\mu_i}{\mu_j})^{0.5}(\frac{M_j}{M_i})^{0.5}]^2}{2\sqrt{2}(1+\frac{M_j}{M_i})^{0.5}} \qquad (S5)$$

693   in which μ_p is the correction term for the viscosity variation as its changes

694   with pressure and given by

695    $\mu_p = 1.1 \times 10^{-8}(e^{1.439\rho_{rm}} - e^{-1.111\rho_{rm}^{1.858}}) \times M_m^{0.5} \cdot \frac{P_{cm}^{2/3}}{T_{cm}^{1/6}}$ (S6)

696   **SI2. Gas Transport in GPT**

697   From Eq. (2A), the transport of gas in the GPT with the "unipore" model

698   under a small pressure gradient in a spherical coordinate system with laminar

699   flow is based on the Darcy-type relation. Because the transfer rate of the fluid

700   is proportional to the concentration gradient, this process can be expressed as:

701
$$\frac{\partial \rho_p}{\partial t} = \frac{k}{c_t \phi_f \mu}(\frac{2}{r}\frac{\partial \rho_p}{\partial r} + \frac{\partial^2 \rho_p}{\partial r^2}) \qquad (S7)$$

702   We set

703    $$k_s = \frac{k}{\mu} \qquad \text{(S8)}$$

704    $$K_a = \frac{k_s}{c_t \phi_f} \qquad \text{(S9)}$$

705   Then, Eq. (S7) becomes:

706    $$\frac{\partial \rho_p}{\partial t} = K_a \left(\frac{2}{r} \frac{\partial \rho_p}{\partial r} + \frac{\partial^2 \rho_p}{\partial r^2} \right) \text{ or } \frac{\partial}{\partial t}(\rho_p r) = K_a \frac{\partial^2}{\partial r^2}(\rho_p r) \qquad \text{(S10)}$$

707   We next introduce the following dimensionless variables:

708    $$U_s = \frac{r}{R} \frac{(\rho_{ps} - \rho_{p2})}{(\rho_{p0} - \rho_{p2})} \qquad \text{(S11)}$$

709    $$U_f = \frac{\rho_{pf} - \rho_{p2}}{\rho_{p0} - \rho_{p2}} \qquad \text{(S12)}$$

710    $$\xi = \frac{r}{R} \qquad \text{(S13)}$$

711    $$\tau = \frac{K_a t}{R^2} \qquad \text{(S14)}$$

712   where ρ_1 and ρ_2 are the gas density in the reference and sample cells, and

713   ρ_0 is the gas density outside the connected pore volume (the gas has flowed

714   from the reference into sample cells but not into samples), and ρ_0 is given by

715    $$\rho_0 = \frac{V_1 \rho_1 + (V_2 - V_b) \rho_2}{V_c} \qquad \text{(S15)}$$

716   where V_1 is the reference cell volume, V_2 is the sample cell volume, V_b is

717   the bulk volume of the sample, V_c is the total void volume of the system

718   minus V_b where $V_c = V_1 + V_2 - V_b$.

719   If the bulk density of the sample is ρ_b and the total mass of the sample is

720   M_s, then the total number of sample particles N is:

721
$$N = \frac{M_s}{\frac{4}{3}\pi R_a{}^3 \rho_b} \tag{S16}$$

722 Based on Darcy's law, the gas flow into a sample Q is:

723
$$Q = -4\pi R^2 (k_s \frac{\partial p}{\partial r}) N = -\frac{3}{R}\frac{M_s}{\rho_b} k_s \frac{\partial p}{\partial r} \tag{S17}$$

724 According to mass conservation and in combination with Eq. (S17), for

725 $t > 0$ and $r = R_a$, we have

726
$$-\frac{3}{R} V_b K_a c_t \phi_f \frac{\partial p}{\partial r} \rho_s = V_c \frac{\partial \rho_f}{\partial t} \tag{S18}$$

727 Substituting Eq. (1C) into Eq. (S18), the boundary condition of Eq. (S10),

728 for $\xi = 1$, is:

729
$$-\frac{3}{R} V_b K_a \phi_f \frac{\partial \rho_s}{\partial r} = V_c \frac{\partial \rho_f}{\partial t} \tag{S19}$$

730 Substituting dimensionless variables into Eq. (S10) yields:

731
$$\frac{\partial U_s}{\partial \tau} = \frac{\partial^2 U_s}{\partial \xi^2} \tag{S20}$$

732 By defining parameter K_c as:

733
$$K_c = \frac{V_c}{V_b \phi_f} \tag{S21}$$

734 –the boundary condition of Eq. (S19) becomes:

735
$$\frac{\partial U_f}{\partial \tau} = -\frac{3}{K_c} \left(\frac{\partial U_s}{\partial \xi} - \frac{U_s}{\xi} \right) \tag{S22}$$

736 From Eq. (S21), K_c represents the ratio of gas storage capacity of the total

737 void volume of system to the pore volume (including both adsorption and non-

738 adsorption volume) of sample.

739 The initial condition of Eq. (S20), for $\tau = 0$, is:

740                     $$\text{when } 0 \le \xi < 1, U_s = 0 \qquad \text{(S23)}$$

741   For $\tau > 0$:

742                     $$\xi = 0, U_s = 0 \qquad \text{(S24)}$$

743                     $$\xi = 1, U_s = U_f = 1 \qquad \text{(S25)}$$

744                     $$\frac{\partial U_s}{\partial \tau} = \frac{\partial^2 U_s}{\partial \xi^2}, 0 < \xi < 1 \qquad \text{(S26)}$$

745   Replacing the Heaviside operator $p = \partial/\partial \tau$ as $p = -s^2$, Eq. (S20) and

746   Eq. (S22) then become:

747                     $$\frac{\partial^2 U_s}{\partial \xi^2} + s^2 U_s = 0 \Big|_{U_s=0, \xi=0} \qquad \text{(S27)}$$

748                     $$\alpha^2 (U_s - 1) = \frac{3}{K_c} \left(\frac{\partial U_s}{\partial \xi} - \frac{U_s}{\xi} \right) \Big|_{\xi=1} \qquad \text{(S28)}$$

749   For these first- and second-order ordinary differential equations, we can

750   solve Eqs. (S27) and (S28) as:

751                     $$U_s = \frac{\alpha^2 \sin \alpha \xi}{\frac{3}{K_c}(\sin \alpha - \alpha \cos \alpha) + \alpha^2 \sin \alpha} \qquad \text{(S29)}$$

752   In Eq. (S29), α_n are the roots of Eq. (S30):

753                     $$\tan \alpha = \frac{3\alpha}{3 + \alpha^2 K_c} \qquad \text{(S30)}$$

754   Defining the numerator and denominator of Eq. (S29) as functions

755    $f(\alpha)$ and $F(\alpha)$, U_s can be expressed as:

756                     $$U_s = \lim_{\alpha \to 0} F \frac{f(\alpha)}{F(\alpha)} + 2 \sum_{n=1}^{\infty} \frac{f(\alpha_n)}{\alpha_n F'(\alpha_n)} e^{-\alpha_n^2 \tau} \qquad \text{(S31)}$$

757

758   **SI2-1: Solution for the Limited K_c Value**

759   Under the condition of limited K_c value, Eq. (S20) is solved with the

760   boundary condition of $0 < \xi < 1$ at time t, and the gas state on the grain

761   surface is initially at equilibrium with the gas outside. Using the Laplace

762   transform, Eq. (S31) is given as (the Laplace transform part can be found in

763   APPENDIX V of Carslaw & Jaeger, 1959) (Brokaw, 1968; Sutherland, 1895):

764
$$U_s = \frac{\xi K_c}{K_c+1} + 6\sum_{n=1}^{\infty} \frac{\sin \xi \alpha_n}{\sin \alpha_n} \frac{K_c e^{-\alpha_n^2 \tau}}{9(K_c+1)+\alpha_n^2 K_c^2} \qquad (S32)$$

765   As the pressure transducer detects the pressure in the reference cell, with

766   the boundary condition $U_f = U_s|_{\xi=1}$, we can calculate U_f as:

767
$$U_f = \frac{K_c}{1+K_c} + 6\sum_{n=1}^{\infty} \frac{K_c e^{-\alpha_n^2 \tau}}{9(K_c+1)+\alpha_n^2 K_c^2} \qquad (S33)$$

768   For a convenient expression of α_n through logarithmic equation, Eq. (S33)

769   can be transformed as:

770
$$(1 - U_f)(1 + K_c) = 1 - 6\sum_{n=1}^{\infty} \frac{K_c(1+K_c)e^{-\alpha_n^2 \tau}}{9(K_c+1)+\alpha_n^2 K_c^2} \qquad (S34)$$

771   The left side of Eq. (S34) clearly has a physical meaning for the state of

772   gas transport outside the sample, and we define $(1 - U_f)(1 + K_c)$ as F_f,

773   which is less than, but infinitely close to, 1. Parameter F_f represents (1) the

774   fraction of final gas transfer of V_c which has taken place by time t, which can

775   be interpreted as the net change in the density of gas at time t to time infinity

776   as Eq. (S35), or (2) as the fractional approach of the gas density to its steady-

777   state in terms of dimensionless variables as Eq. (S36).

$$F_f = \frac{\rho_{p0} - \rho_{pf}}{\rho_{p0} - \rho_{f\infty}} \text{ or} \tag{S35}$$

778

$$F_f = \frac{1 - U_f}{1 - U_\infty} = \frac{\rho_{p0} - \rho_{pf}}{\rho_{p0} - \rho_{p2}}(1 + K_c) \tag{S36}$$

779

780   where for $\tau \to \infty$, the result of U_f and $\rho_{f\infty}$ would tend to be the limiting

781   value:

$$U_\infty = U_s = U_f \xi = \left.\frac{\xi K_c}{1 + K_c}\right|_{\xi=1} \tag{S37}$$

782

$$\rho_{f\infty} = \frac{V_1 \rho_1 + (V_2 - V_s)\rho_2}{V_1 + V_2 - V_s} = \frac{K_c}{1 + K_c}(\rho_{p0} - \rho_{p2}) + \rho_{p2} \tag{S38}$$

783

784   Thus, Eq. (S34) can be expressed as:

$$F_f = 1 - 6\sum_{n=1}^{\infty} \frac{K_c(1 + K_c)e^{-\alpha n^2 \tau}}{9(K_c + 1) + \alpha_n^2 K_c^2} \tag{S39}$$

785

786   For calculating the permeability, Eq. (S39) can be linearized as a function

787   of time as there are no variables other than the exponential part:

$$ln(1 - F_f) = f_1 - s_1 t \tag{S40}$$

788

789   where f_1 is the intercept for the y-axis of function (S40):

$$f_1 = ln[\frac{6K_c(1 + K_c)}{9(1 + K_c) + \alpha_1^2 K_c^2}] \tag{S41}$$

790

791   The slope s_1 can be captured by the fitted line of the linear segment, and

792   α_1 is the first solution of Eq. (S30):

$$s_1 = \frac{\alpha_1^2 K_a}{R_a^2} \tag{S42}$$

793

794   Thus, the permeability can be calculated as:

$$k = \frac{R_a^2 \mu c_t \phi_f s_1}{\alpha_1^2} \tag{S43}$$

795

SI2-2: Solution for K_c Goes to Infinity

When V_c has an infinite volume compared to the void volume in a sample, which means that the density of gas in V_c would be kept at ρ_{p0}, and α would approach $n\pi$ in Eq. (S30), then Eq. (S32) can be transformed as:

$$U_S = \xi + \frac{2}{\pi}\sum_{n=1}^{\infty}(-1)^n \frac{\sin n\pi\xi}{n}e^{-(n\pi)^2\tau} \qquad (S44)$$

In this situation, $U_f = 1$, and as the gas density would be maintained at the initial state at ρ_{p0}, it would be a familiar case in diffusion kinetics problems with the uptake rate of F_f to be expressed as F_s in V_b (Barrer, 1941):

$$F_S = \frac{\rho_{sav}}{\rho_{s\infty}} \qquad (S45)$$

where ρ_{sav} is the average value of ρ_{sr} in the grain, and $\rho_{s\infty}$ is the maximum value of ρ_{sr}:

$$\rho_{sr} = \rho_{ps} - \rho_{p2}, \quad \rho_{s\infty} = \rho_{p0} - \rho_{p2} \qquad (S46)$$

The value of ρ_{sr} in the grain is:

$$\rho_{sav} = \frac{3}{R^3}\int_0^R \rho_{sr}r^2\,d\,r \qquad (S47)$$

Then F_s becomes:

$$F_S = \frac{3}{R^3}\int_0^R \frac{U_S}{\xi}r^2\,d\,r \qquad (S48)$$

Substituting Eq. (S44) into Eq. (S48), we can calculate:

$$F_s = 1 - \frac{6}{\pi^2} \sum_{n=1}^{\infty} \frac{e^{-(n\pi)^2 \tau}}{n^2} \qquad \text{(S49)}$$

Similar to Eq. (S39), Eq. (S49) can also be linearized to calculate the permeability in τ from the fitted slope. For $\tau \geq 0.08$, Eq. (S49) can be reduced as:

$$F_s = 1 - \frac{6}{\pi^2} e^{-\pi^2 \tau} \qquad \text{(S50)}$$

When t is small enough (for $\tau \leq 0.002$), Eq.(S49) can be transformed into Eq. (S51).

$$F_s = 6 \sqrt{\frac{\tau}{\pi}} \qquad \text{(S51)}$$

As F_s is a special solution of F_f with the case of K_c goes to infinity, we can arrive at:

$$F_s = F_f = (1 - U_f)(1 + K_c) \qquad \text{(S52)}$$

For testing the ultra-low permeability rocks using granular samples when K_c goes to infinity, Eq. (S50) and Eq. (S51) can be selected using different τ values.

From the fitted slope s_2 of function $ln(1 - F_s)$ from Eq. (S50), we can then derive the permeability:

$$k = \frac{R_a{}^2 \mu c_t \phi_f s_2}{\pi^2} \qquad \text{(S53)}$$

The results of Eq. (S53) are very similar to Eq. (S43) as the first solution for Eq. (S30) is very close to π.

832 From the fitted slope s_3 of function $F_s{}^2$ from Eq. (S51), we can derive

833 the permeability:

834 $$k = \frac{\pi R_a{}^2 \mu c_t \phi_f s_3}{36} \qquad\qquad \text{(S54)}$$

835

836 **SI3. A Case of Data Processing for GPT**

837 We show here an illustration of the data processing procedure for the GPT

838 with a molecular sieve sample (https://www.acsmaterial.com/molecular-

839 sieves-5a.html). This material consists of grains of 2 mm in Diameter with a

840 porosity of 26.28%, and a uniform pore-throat size of 5Å in Diameter, with a

841 particle density of 2.96 g/cm^3. For a 45 g sample, the K_c value is 19.4 from

842 Eq. (S21), and therefore 4.9% of the density ratio $(1 - K_f)$ is available for

843 mass transfer from Eq. (1G).

844 The experimental data were captured under a strict temperature control and

845 unitary-gas environment, along with a precise measurement of barometric

846 pressure. The experiment was run twice, and after the data were collected, 1)

847 we made a rough evaluation of the "Penetration Zone" of this sample based on

848 Figs. 5-6. For this molecular sieve sample, the "Penetration Zone" is shown in

849 Fig. S1, and the mass transfer in unit time more conforming to a linear state

850 (shown as Fig. 5) over a large time range, especially at 100-300s; 2) data in

851 the selected range (100-300s) were fitted respectively for the slope from Fig.

852   S2, then slopes were compiled in Table SI3-1; 3) permeabilities were

853   calculated using the slope of the fitted curve, and all results for LLT, ILT and

854   IET are also shown in Table SI3-1; 4) the results were checked with their

855   dimensionless times to verify whether the early- or late-time solutions were

856   used correctly. Table SI3-1 clearly shows that the results of IET should be

857   selected for this sample, as the dimensionless time is less than 0.024. Note that

858   the data fluctuation shown here was from a high resolution ($\pm$0.1% for 250

859   psi) pressure sensor without undergoing a smoothing process; meanwhile, for

860   data in the 100-200, 200-300, and 300-400 seconds of experimental duration,

861   100, 200, and 300 seconds respectively were used to calculate the

862   dimensionless times for the results in Table SI3-1.

863   In addition, the validity of the permeability obtained needs to be verified by

864   using the time interval employed in data fitting and the calculated permeability

865   results to calculate the τ (Table SI3-1). If the dimensionless time is less than

866   0.024 (as occurred for the case of molecular sieve), the IET solution is selected;

867   if the dimensionless time is greater than 0.024 and K_c is greater than 10, the

868   ILT solution is used; if τ is greater than 0.024 and K_c is less than 10, then

869   the LLT solution is employed. However, for sample sizes smaller than 1.27

870   mm, Conflicting Results (described in Table 1) occur, and results from this

871   situation are not recommended due to poor data quality.

872
Table SI3-1. Permeability results of molecular sieve from LLT, IET and ILT

Fitting range (s)	LLT (m²)	τ -LLT	IET(m²)	τ -IET	ILT (m²)	τ -ILT	Slope-LLT	Slope-IET	Slope-ILT
100-200	5.60E-22	0.004	1.02E-21	0.007	5.00E-22	0.003	0.0004	0.0007	0.0004
200-300	4.20E-22	0.006	5.81E-22	0.008	3.75E-22	0.005	0.0003	0.0004	0.0003
300-400	2.80E-22	0.006	4.36E-22	0.009	2.50E-22	0.005	0.0002	0.0003	0.0002
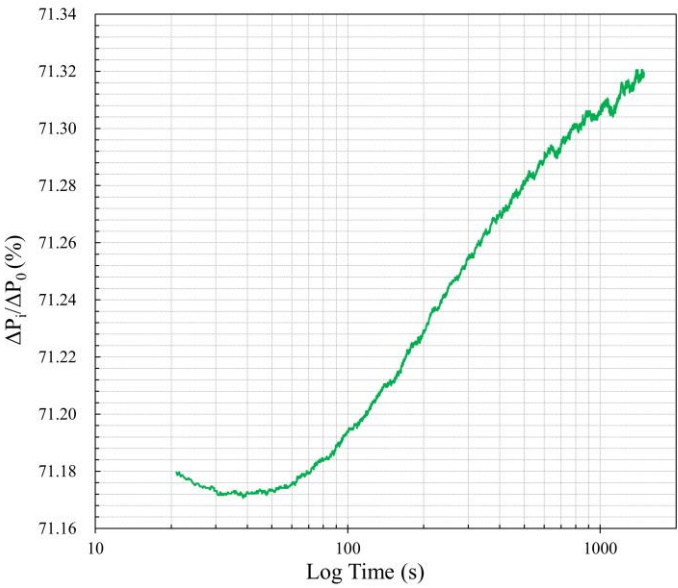
873

874   Fig. S1. Unit pressure change varying with experimental time.

875
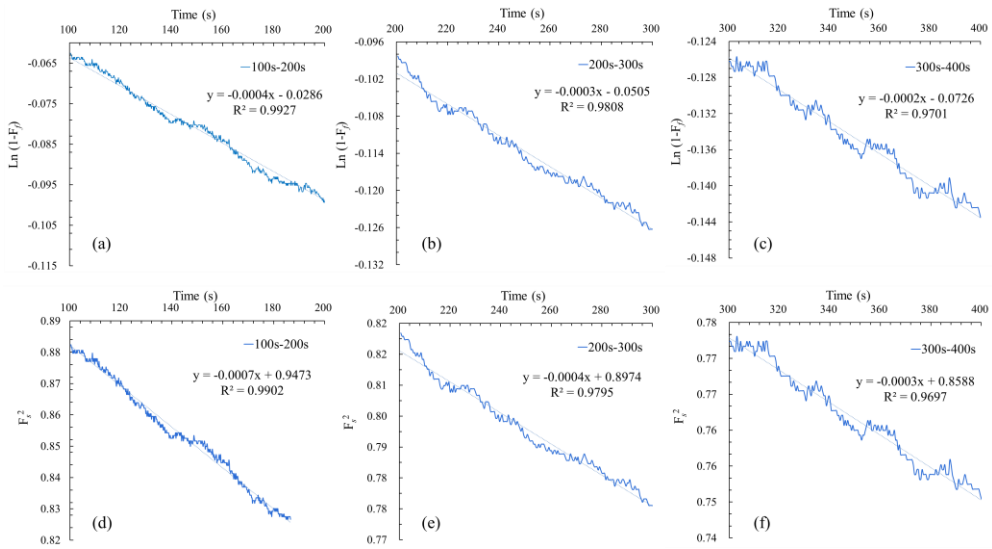
876
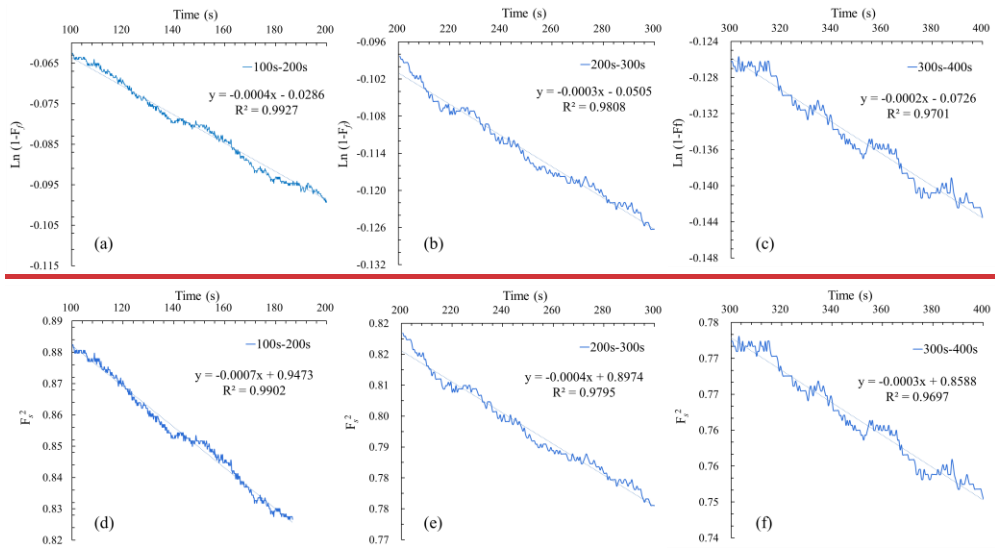
Fig. S2. Fitted slopes for each solution; (a) to (c) are results of LLT and ILT, while (d) to (f) of IET.

SI4. Equipment and samples

The experimental setup in the GPT presented in this study is based on the GRI-95/0496 protocols (Guidry et al., 1996) and the SMP-200 guidelines from Core Laboratories with the gas expansion approach (shown in Fig. S3). In this work, gases (He, Ar, N_2, or CO_2) with different molecular sizes and sorption capacities were tested using two shale core samples (X1, X2) from an oil-producing lacustrine formation in the Songliao Basin, China. X1 is used for sample size study where X2 used for experiment with different gas. Also, we used the molecular sieve to exhibit the practical utilization of the GPT method in SI3. We gently crushed the intact samples with mortar and ground to

890 different granular sizes from 0.34 mm to 5.18 mm through a stack of sieves

891 (named here as Size X: 8 mm to #8 mesh; GRI+: #8-#12 mesh; Size A: #12-

892 #20 mesh; GRI: #20-#35 mesh; Size B: #35-#80 mesh).

893
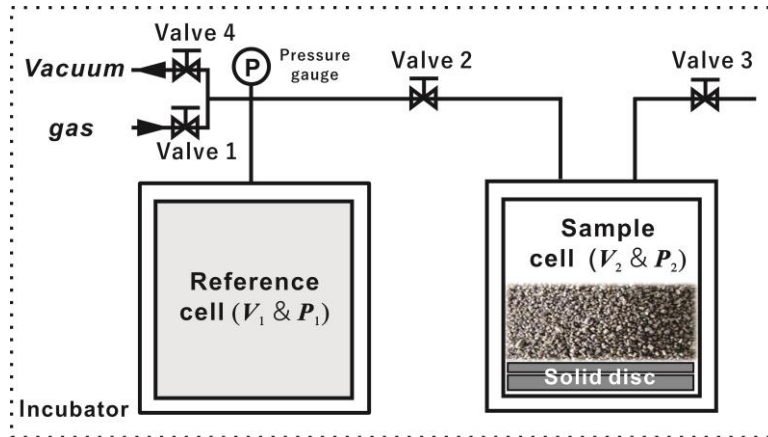
894 Fig. S3. Scheme of the GPT experiment for granular samples with all the cells and

895 supplies placed inside an incubator for temperature control.

896 After loading each sample, related accessories (e.g., solid discs or balls for

897 volume control; and hence porosity, sample mass, and solution-related) were

898 placed below samples inside the cell (Fig. S3). Next, valves 1 and 3 were

899 closed, then valves 2 and 4 were opened for air evacuation. Using a precise

900 pressure gauge connected to the reference cell shown in Fig. S3 we monitored

901 changes in the pressure. The evacuation time typically lasted at least 15-30

902 min, and then the system was allowed to stabilize for another 15 min. As the

903 moisture content of the samples significantly influences the final vacuum, the

904 samples were placed into the sample cell immediately after removal from the

905   drying oven set at 60°C for two days and cooling in a low-humidity desiccator.

906   The experiments were conducted at the temperature of 35°C by placing the

907   SMP-200 inside an incubator equipped with a high precision temperature-

908   humidity sensor to monitor changes. This is to ensure that the system

909   temperature was always stable (0.05°C over at least 45 mins of experimental

910   duration). For temperature monitoring, after evacuation, we closed valves 3

911   and 4 followed by opening valves 1 and 2 (shown in Fig. S3) and monitoring

912   the heat convection and conduction in the system with the pressure gauge.

913   Normally, the sample was placed inside the sample cell in less than 30 sec

914   after opening the incubator and remained at least 45 min for the gas pressure

915   to stabilize before the pressure decay test. After the pressure was stabilized

916   (0.005 psi for an experimental pulse pressure of 200 psi), it was deemed that

917   there was no appreciable additional flow due to temperature variation in the

918   system, as indicated by the rebound of the pressure decay curve. After reaching

919   a unitary gas condition and stable temperature in the GPT experiment, valves

920   2 and 4 were closed, and the reference cell was filled with the probing gas

921   (mostly non-reactive helium) at 200 psi. Valve 2 was then opened to release

922   the pressure in the reference cell into the void volume in the sample cell, and

923   the pressure decay for both reference and sample cells were recorded over time.

924   **SI5. Experimental conditions**

925   We performed leakage tests by measuring the pressure variation with non-

926   porous solids, such as steel balls, as any leakage would cause pressure

927   variations and, accordingly, errors in permeability measurements of tight

928   porous samples (Heller et al., 2014). Before the data from porous samples were

929   analyzed, the leakage pressure from the steel ball experiment was subtracted

930   from the sample data to correct the modest (<5% of the pressure levels used

931   for permeability analyses) leakage effect.

932   The need for a unitary gas environment (a single gas used in both reference

933   and sample cells) is needed to successfully measure permeability via the GPT

934   method. The relative movement of gas molecules in the mass transfer process

935   is driven by the gas density gradient in the system. During gas transport, the

936   pressure variance was recorded and used to obtain the permeability coefficient.

937   However, when the gas in both cells is different, e.g., helium in the reference

938   and air in the sample cells, the mathematical analysis requires a complicated

939   correction accounting for the mean molar mass and the average gas dynamic

940   viscosity of the gas mixture. In this study, we present the calculation with the

941   viscosity of mixed gases for the GPT in the SI1. Since the mixed gas

942   environment is not recommended, air evacuation should be used for a well-

943   controlled unitary gas environment in the GPT.

944   A stable temperature is another critical point to ensure the success of the

GPT experiment. A sensitive pressure transducer in combination with the ideal gas law, used to establish the relationship between pressure and gas volume change, would be a much more convenient and precise way than the gas flow meter to determine the gas permeability considering the measurement accuracy. According to Amonton's law (Gao et al., 2004), the kinetic energy of gas molecules is determined by the temperature, and any changes would alter the molecular collision force causing a pressure variation and a volumetric error. The GPT experiments were run two or three times on the same sample, and the sample skeletal density at the end of the experiment were obtained to check the overall indication of leakage and temperature control. The experimental data with relatively large and stable skeletal density (mostly the last run, from small but appreciable pressure change to reach stable values) were used.

References:

Abdassah, D., Ershaghi, I., 1986. Triple-porosity systems for representing naturally fractured reservoirs. SPE Formation Evaluation 1(02), 113-127.

Barrer, R.M., 1941. Diffusion in and through solids, Рипол Классик.

Bibby, R., 1981. Mass transport of solutes in dual‐porosity media. Water Resour. Res. 17(4), 1075-1081.

Bock, H., Dehandschutter, B., Martin, C.D., Mazurek, M., De Haller, A., Skoczylas, F., Davy, C., 2010. Self-sealing of fractures in argillaceous formations in the context of geological disposal of radioactive waste.

Brace, W.F., Walsh, J.B., Frangos, W.T., 1968. Permeability of granite under high pressure. Journal of Geophysical Research 73(6), 2225-2236.

Brokaw, R.S., 1968. Viscosity of gas mixtures, National Aeronautics and Space Administration.

Busch, A., Alles, S., Gensterblum, Y., Prinz, D., Dewhurst, D.N., Raven, M.D., Stanjek, H., Krooss, B.M., 2008. Carbon dioxide storage potential of shales. Int. J. Greenh. Gas Control 2(3), 297-308.

Carslaw, H.S., Jaeger, J.C., 1959. Conduction of heat in solids.

Chen, X., Pfender, E., 1983. Effect of the Knudsen number on heat transfer to a particle immersed into a thermal plasma. Plasma Chem. Plasma Process. 3(1), 97-113.

Civan, F., Devegowda, D., Sigal, R.F., 2013. Critical evaluation and improvement of methods for determination of matrix permeability of shale, Society of Petroleum Engineers.

Cui, X., Bustin, A., Bustin, R.M., 2009. Measurements of gas permeability and diffusivity of tight reservoir rocks: different approaches and their applications. Geofluids 9(3), 208-223.

Devegowda, D., 2015. Comparison of shale permeability to gas determined by pressure-pulse transmission testing of core plugs and crushed samples, Unconventional Resources Technology Conference (URTEC).

Egermann, P., Lenormand, R., Longeron, D.G., Zarcone, C., 2005. A fast and direct method of permeability measurements on drill cuttings. Spe Reserv. Eval. Eng. 8(04), 269-275.

Fakher, S., Abdelaal, H., Elgahawy, Y., El-Tonbary, A., 2020. A Review of Long-Term Carbon Dioxide Storage in Shale Reservoirs, OnePetro.

Gao, J., Luedtke, W.D., Gourdon, D., Ruths, M., Israelachvili, J.N., Landman, U., 2004. Frictional forces and Amontons' law: from the molecular to the macroscopic scale, ACS Publications.

Gensterblum, Y., Ghanizadeh, A., Cuss, R.J., Amann-Hildenbrand, A., Krooss, B.M., Clarkson, C.R., Harrington, J.F., Zoback, M.D., 2015. Gas transport and storage capacity

in shale gas reservoirs – A review. Part A: Transport processes. Journal of Unconventional Oil and Gas Resources 12, 87-122.

Ghanbarian, B., 2022a. Estimating the scale dependence of permeability at pore and core scales: Incorporating effects of porosity and finite size. Adv. Water Resour. 161, 104123.

Ghanbarian, B., 2022b. Scale dependence of tortuosity and diffusion: Finite-size scaling analysis. J. Contam. Hydrol. 245, 103953.

Ghanbarian, B., Hunt, A.G., Daigle, H., 2016. Fluid flow in porous media with rough pore‐solid interface. Water Resour. Res. 52(3), 2045-2058.

Guidry, K., Luffel, D., Curtis, J., 1996. Development of laboratory and petrophysical techniques for evaluating shale reservoirs. Final technical report, October 1986-September 1993, ResTech Houston, Inc., TX (United States).

Gutierrez, M., Øino, L.E., Nygaard, R., 2000. Stress-dependent permeability of a de-mineralised fracture in shale. Mar. Pet. Geol. 17(8), 895-907.

Haggerty, R., Gorelick, S.M., 1995. Multiple‐rate mass transfer for modeling diffusion and surface reactions in media with pore‐scale heterogeneity. Water Resour. Res. 31(10), 2383-2400.

Haskett, S.E., Narahara, G.M., Holditch, S.A., 1988. A method for simultaneous determination of permeability and porosity in low-permeability cores. SPE formation evaluation 3(03), 651-658.

Haszeldine, S., Lu, J., Wilkinson, M., Macleod, G., 2006. Long-timescale interaction of CO_2 storage with reservoir and seal: Miller and Brae natural analogue fields North Sea. Greenhouse Gas Control Technology 8.

Heller, R., Vermylen, J., Zoback, M., 2014. Experimental investigation of matrix permeability of gas shalesExperimental Investigation of Matrix Permeability of Gas Shales. Aapg Bull. 98(5), 975-995.

Hu, Q., Ewing, R.P., Dultz, S., 2012. Low pore connectivity in natural rock. J. Contam. Hydrol. 133, 76-83.

Hu, Q., Ewing, R.P., Rowe, H.D., 2015. Low nanopore connectivity limits gas production in Barnett formation. Journal of Geophysical Research: Solid Earth 120(12), 8073-8087.

Huenges, E., 2016., pp. 743-761, Elsevier.

Javadpour, F., 2009. Nanopores and apparent permeability of gas flow in mudrocks (shales and siltstone). Journal of Canadian Petroleum Technology 48(08), 16-21.

Jia, B., Tsau, J., Barati, R., Zhang, F., 2019. Impact of Heterogeneity on the Transient Gas Flow Process in Tight Rock. Energies 12(18), 3559.

Kamath, J., 1992. Evaluation of accuracy of estimating air permeability from mercury-injection data. SPE Formation evaluation 7(04), 304-310.

Khosrokhavar, R., 2016. Shale gas formations and their potential for carbon storage: opportunities and outlook. Mechanisms for CO2 Sequestration in Geological Formations and Enhanced Gas Recovery, 67-86.

Kim, C., Jang, H., Lee, J., 2015. Experimental investigation on the characteristics of gas diffusion in shale gas reservoir using porosity and permeability of nanopore scale. J. Pet. Sci. Eng. 133, 226-237.

Kim, J., Kwon, S., Sanchez, M., Cho, G., 2011. Geological storage of high level nuclear waste. Ksce J. Civ. Eng. 15(4), 721-737.

Liu, W., Li, Y., Yang, C., Daemen, J.J., Yang, Y., Zhang, G., 2015. Permeability characteristics of mudstone cap rock and interlayers in bedded salt formations and tightness assessment for underground gas storage caverns. Eng. Geol. 193, 212-223.

Lu, J., Wilkinson, M., Haszeldine, R.S., Fallick, A.E., 2009. Long-term performance of a mudrock seal in natural CO_2 storage. Geology 37(1), 35-38.

Luffel, D.L., Hopkins, C.W., Schettler Jr, P.D., 1993. Matrix permeability measurement of gas productive shales, Society of Petroleum Engineers.

Neuzil, C.E., 1986. Groundwater flow in low‐permeability environments. Water Resour. Res. 22(8), 1163-1195.

Neuzil, C.E., 2013. Can shale safely host US nuclear waste? Eos, Transactions American Geophysical Union 94(30), 261-262.

Peng, S., Loucks, B., 2016. Permeability measurements in mudrocks using gas-expansion methods on plug and crushed-rock samples. Mar. Pet. Geol. 73, 299-310.

Pini, R., 2014. Assessing the adsorption properties of mudrocks for CO_2 sequestration. Energy Procedia 63, 5556-5561.

Profice, S., Lasseux, D., Jannot, Y., Jebara, N., Hamon, G., 2012. Permeability, porosity and klinkenberg coefficien determination on crushed porous media. Petrophysics 53(06), 430-438.

Rasmuson, A., 1985. The effect of particles of variable size, shape and properties on the dynamics of fixed beds. Chem. Eng. Sci. 40(4), 621-629.

Roy, S., Raju, R., Chuang, H.F., Cruden, B.A., Meyyappan, M., 2003. Modeling gas flow through microchannels and nanopores. J. Appl. Phys. 93(8), 4870-4879.

Ruthven, D.M., 1984. Principles of adsorption and adsorption processes, John Wiley & Sons.

Ruthven, D.M., Loughlin, K.F., 1971. The effect of crystallite shape and size distribution on diffusion measurements in molecular sieves. Chem. Eng. Sci. 26(5), 577-584.

Sutherland, W., 1895. XXXVII. The viscosity of mixed gases. The London, Edinburgh, and Dublin Philosophical Magazine and Journal of Science 40(246), 421-431.

Tarkowski, R., 2019. Underground hydrogen storage: Characteristics and prospects.

1071   Renewable and Sustainable Energy Reviews 105, 86-94.

1072 Wu, T., Zhang, D., Li, X., 2020. A radial differential pressure decay method with micro-plug

1073   samples for determining the apparent permeability of shale matrix. J. Nat. Gas Sci. Eng.

1074   74, 103126.

1075 Yang, M., Annable, M.D., Jawitz, J.W., 2015. Back diffusion from thin low permeability

1076   zones. Environ. Sci. Technol. 49(1), 415-422.

1077 Zhang, J.J., Liu, H., Boudjatit, M., 2020. Matrix permeability measurement from fractured

1078   unconventional source-rock samples: Method and application. J. Contam. Hydrol.,

1079   103663.

1080 Zhang, T., Hu, Q., Chen, W., Gao, Y., Feng, X., Wang, G., 2021. Analyses of True-Triaxial

1081   Hydraulic Fracturing of Granite Samples for an Enhanced Geothermal System.

1082   Lithosphere 2021(Special 5).

1083 Zhang, T., Zhou, W., Hu, Q., Xu, H., Zhao, J., Zhang, C., 2021. A pulse-decay method for

1084   low permeability analyses of granular porous media: Mathematical solutions and

1085   experimental methodologies.

1086